Critical behavior, magnetic phase diagram, and magnetic entropy change of MnSb$_2$Te$_4$

Xiaojun Yang ⊙,[*] Junxiao Pan, Xiangyu He, and Dongliang Chu

College of Physics and Electronic Information, Luoyang Normal University, Luoyang 471022, China

The magnetic properties of single-crystal MnSb$_2$Te$_4$ were thoroughly investigated. The $M(T)$ curves exhibit anisotropic magnetic behaviors with the c axis as the easy axis in low temperature, while Curie-Weiss fitting curves show an isotropic behavior at high temperature. The evaluated Rhodes-Wohlfarth ratio of 2.25 (2.22) for $H//ab$ ($H//c$) demonstrates an itinerant high-field ferromagnetic state. Critical exponents $\beta = 0.441(9)$ with $T_C = 19.4(1)$ K and $\gamma = 1.108(13)$ with $T_C = 19.3(1)$ K are acquired by the modified Arrott plots, whereas $\delta = 3.52(1)$ is achieved by a critical isotherm analysis at $T_C = 19.4$ K, exhibiting three-dimensional critical behavior and complex magnetic interaction. A detailed H-T phase diagram containing antiferromagnetic, canted antiferromagnetic, and ferromagnetic states is constructed, where two triple points ($\sim$310 Oe at 19.4 K and $\sim$1970 Oe at 19.4 K) are achieved. Additionally, the magnetic entropy change ΔS_M is evaluated with $-\Delta S_M^{\max}$ reaching 2.20 J kg^{-1} K^{-1} in the ab plane and 2.20 J kg^{-1} K^{-1} along the c axis at $H = 70$ kOe. The rotating magnetic entropy change $-\Delta S_M^R(T,H)$ is $\sim$0 J kg^{-1} K^{-1} at $T > 39$ K, displaying a nearly isotropic behavior well above T_C, consistent with the above Curie-Weiss fitting; and $-\Delta S_M^R$ is less than 0.24 J kg^{-1} K^{-1} at low temperature, demonstrating weak anisotropy.

I. INTRODUCTION

Intrinsic magnetic topological materials, which are stoichiometric topological materials with an inherent magnetic order, have attracted researchers' attention due to their extraordinary properties, e.g., anomalous surface or edge states [1–4], unconventional bulk transport properties [5–7], and the coupling between the magnetism and topological states [8–13]. Recently, extensive works have been focused on the layered van der Waals (vdW) compound MnBi$_2$Te$_4$, which is a peculiar intrinsic A-type antiferromagnetic (AFM) topological insulator with Mn ferromagnetic (FM) layers stacked antiferromagnetically along the c axis [11], revealing rich quantum states and exotic phenomena such as an axion insulator phase, a quantum anomalous Hall effect, and a high-temperature Chern insulator phase [8,9,14–18]. In MnBi$_2$Te$_4$, the spin structure could be manipulated by an applied magnetic field, bringing about a complicated magnetic phase diagram, which is related to various topological states [9,19], i.e., an axion state at the AFM ground state and a minimal ideal Weyl semimetal at the spin-polarized FM state.

MnSb$_2$Te$_4$ is isostructural to MnBi$_2$Te$_4$, which crystallizes in a hexagonal structure with the space group of $R\bar{3}m$ (no. 166) [insets of Fig. 1(a)], constructed by septuple layers of Te-Sb-Te-Mn-Te-Sb-Te stacked along the crystallographic c axis via vdW interaction [20–22]. With the Mn-Sb site mixing or application of an external field, the A-type AFM state in MnSb$_2$Te$_4$ can be driven to a FM state [23,24], similar to MnBi$_2$Te$_4$. In MnBi$_2$Te$_4$, a large external magnetic field ($\sim$8 T) is needed to fully polarize the AFM spins into a

forced FM state [25]. A relatively smaller external magnetic field ($\sim$1 T) is required to reach a FM state in MnSb$_2$Te$_4$ [22,24], which is preferred to tune the magnetism and topology by field, and it is appealing for realizing the quantized anomalous Hall conductance at much lower magnetic field or even zero field [26]. Furthermore, the isostructural compound MnSb$_2$Te$_4$ is a better model system for a systematic investigation of the connections among magnetism, topology, and lattice defects due to higher concentrations of the same types of magnetic defects [24]. Compared with the adequate investigations in MnBi$_2$Te$_4$, the sister system MnSb$_2$Te$_4$ has been less explored. This system also possesses rich topological properties, such as the simplest Weyl semimetal with only one pair of Weyl nodes on the threefold rotational axis [20–22], and it deserves thorough investigations. Considering the intimate relation between the topological states and the magnetism [9,19,27,28], a detailed investigation on the magnetic phase diagram of MnSb$_2$Te$_4$ is of essential significance. In particular, the critical behavior of MnSb$_2$Te$_4$, which could provide further insight into the origin of spin dimensionality, magnetic interactions, correlation length, and the spatial decay of the correlation function at criticality [29–32], remains unexplored and is worthy of a comprehensive study.

Due to such fascinating physical properties as possible ideal Weyl fermions and the axion insulator in MnSb$_2$Te$_4$ [20,33], magnetic structures deserve a thorough clarification due to the intimate relation between the charming properties and magnetism. Thus, this work details a comprehensive investigation of the magnetism of the MnSb$_2$Te$_4$ single crystal. The $M(T)$ curves display anisotropic magnetic behaviors, with the magnetic easy axis in the c axis at low temperature, while Curie-Weiss fitting exhibits an isotropic behavior at high temperature. The evaluated Rhodes-Wohlfarth ratio
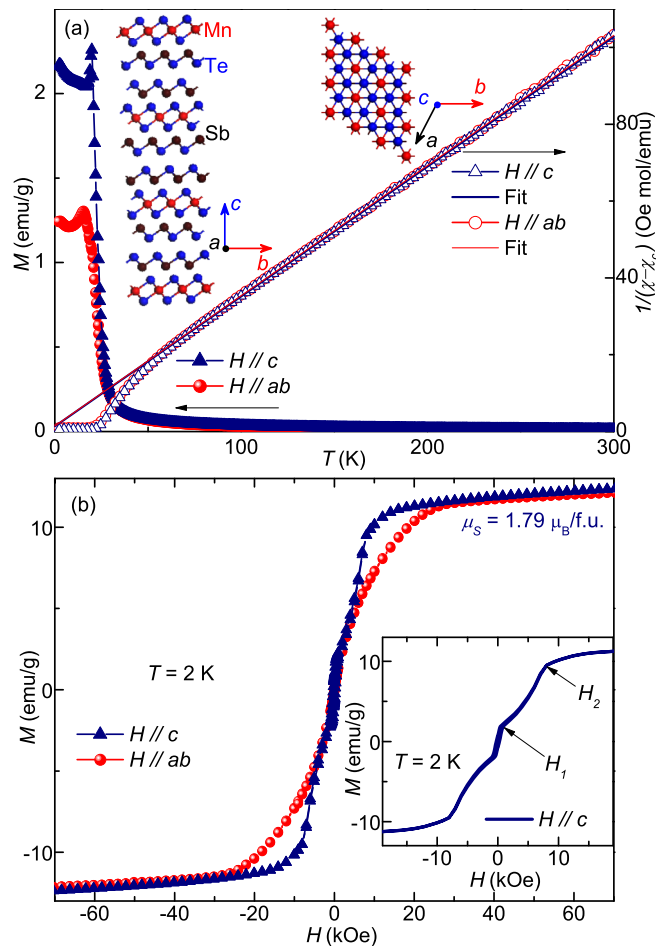
_____
*[*]xiaojunyang01@foxmail.com

FIG. 1. (a) The magnetization (left axis) and $1/(\chi - \chi_c)$ (right axis) as a function of temperature under $H = 1$ kOe for $H//ab$ and $H//c$. Insets: The crystal structure of $MnSb_2Te_4$. (b) The field dependence of isothermal magnetization $M(H)$ curves for $H//ab$ and $H//c$ at $T = 2$ K. Inset: The enlarged $M(H)$ curve for $H//c$ at $T = 2$ K.

(RWR) indicates that the high-field FM state is itinerant. Critical exponents β, γ, and δ are obtained by using various techniques, such as a modified Arrott plot, a Kouvel-Fisher plot, and critical isotherm analysis. The reliability of the deduced critical exponents is checked by the Widom relation and scaling analyses. The obtained critical exponents suggest a three-dimensional (3D) critical behavior and complex magnetic interactions in $MnSb_2Te_4$. An H-T phase graph is constructed in which two field-induced triple points are determined and the magnetic structures are explored. Furthermore, the magnetic entropy change $-\Delta S_M$ is calculated, demonstrating a nearly isotropic behavior well above T_C and weak anisotropy at low temperature.

II. EXPERIMENTAL DETAILS

$MnSb_2Te_4$ single crystals used in this work were fabricated with a Sb-Te self-flux method [22,24]. Starting elements Mn (lump, 99.98%), Sb (grain, 99.9%), and Te (ingot, 99.99%), all from Alfa Aesar, were mixed thoroughly at an atomic ratio of 1 : 10 : 16. The mixtures were placed in an alumina

crucible and sealed in an evacuated quartz tube with a pressure $\leqslant 5 \times 10^{-4}$ Pa. The quartz tube was heated to 1173 K for over 15 h and remained for 12 h in a box furnace. Then, it was slowly cooled down to 893 K in 8100 min, kept for 2 weeks, followed by decanting. The typical size of the grown single crystals is $3 \times 3 \times 0.15$ mm^3. The phase purity of the sample was checked by x-ray diffraction, consistent with previous reports [22,24]. Energy-dispersive x-ray (EDX) spectroscopy collected by an Octane Plus Detector (AMETEX EDAX) indicates an atomic ratio of Mn:Sb:Te = 0.84:2.16:4, exhibiting a small difference from the value of Mn:Sb:Te = 0.82:2.17:4 for the antiferromagnetic sample in Ref. [24]. The magnetization was measured on a commercial magnetic property measurement system (Quantum Design MPMS XL-7). The applied magnetic field H_a is corrected to the internal field as $H_i = H_a - N_d M$, where M and N_d are the magnetization and the demagnetization factor, respectively. The corrected field H_i was used for the critical-behavior analysis.

III. RESULTS AND DISCUSSION

A. Magnetic properties

Magnetization as a function of temperature $M(T)$ from 2 to 300 K under an applied external field of 1 kOe is measured for both $H//ab$ and $H//c$ [the left axis of Fig. 1(a)], in which an AFM transition with a Néel temperature $T_N \sim 19$ K is detected. Apparently, the magnetization at low temperature displays an anisotropic behavior, consistent with the 2D crystal structure in $MnSb_2Te_4$. The magnetization at $H//ab$ is smaller than $H//c$, demonstrating that the magnetic order is preferred along the c axis rather than within the ab plane [22]. Below T_N, the magnetic moments of Mn form an A-type AFM structure, i.e., ferromagnetic a-b planes coupled antiferromagnetically along the c axis [24], similar to the definition in the $MnBi_2Te_4$ system [11,34]. The $M(T)$ curves show upturns at low temperature under $H//ab$ and $H//c$, which is commonly found in A-type antiferromagnets and the origin is still controversial [11,12,35,36]. As displayed on the right axis of Fig. 1(a), the high-temperature paramagnetic (PM) region well obeys the Curie-Weiss law, fitting to the magnetic susceptibility that brings about the effective moment μ_{eff} of $4.86\mu_B$/f.u $(4.87\mu_B$/f.u) and the Weiss temperature of -4.3 K $(-4.0$ K) for $H//ab$ $(H//c)$. The difference of the inverse magnetic susceptibility between the ab plane and the c axis is rather small, implying almost isotropic behavior at high temperature. The negative value of the Weiss temperature suggests an AFM exchange interaction. Figure 1(b) displayed the isothermal magnetizations at $T = 2$ K under $H//ab$ and $H//c$. For $H//c$, two magnetic transitions at $H_1 \sim 1000$ Oe and $H_2 \sim 8000$ Oe are detected, which are also detected in the following isothermal plots of scaled m^2 versus h/m (Fig. 8), and ΔS_M versus H (Fig. 10) curves. We argue that the transitions come from the AFM to canted AFM (CAFM) transition and the CAFM to FM transition similar with $MnBi_2Te_4$ [22,34,37,38], which deserves further in-depth investigation. In the sister compound $MnBi_2Te_4$, it is suggested that the CAFM state is caused by the field-induced suppression of magnetic order [39], the bulk band structure is strongly coupled with the magnetic property, and a net
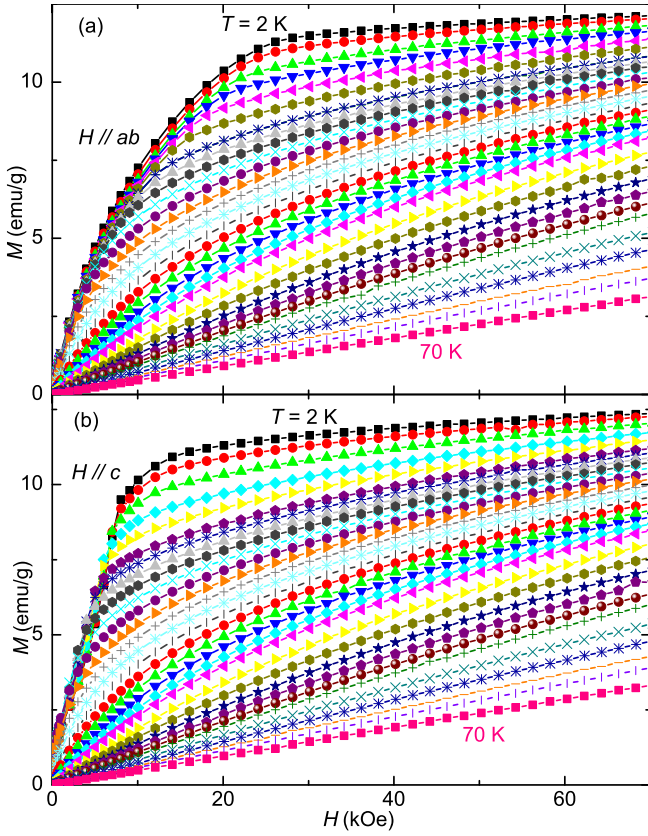
FIG. 2. Field-dependent isothermal magnetization $M(H)$ curves from $T = 2$ to 70 K under (a) $H//ab$ and (b) $H//c$.

Berry curvature in momentum space can be created in the CAFM state [34], making further investigation on the underlying mechanism of the CAFM state in MnSb$_2$Te$_4$ appealing. Compared with MnBi$_2$Te$_4$, the values of the transition field H_1 and H_2 of MnSb$_2$Te$_4$ are much smaller [37,38,40], demonstrating weaker interlayer AFM interactions. For $H//ab$, the critical saturation magnetic field $H \sim 22$ kOe, which is apparently larger than that for $H//c$, further verifying that the c axis is the magnetic easy axis. The saturation moments (μ_s) of MnSb$_2$Te$_4$ for $H//ab$ and $H//c$ can be determined as 1.76μ_B/Mn and 1.79μ_B/Mn, respectively. Detailed isothermal magnetization $M(H)$ from 2 to 70 K with fields up to 70 kOe are also displayed [Figs. 2(a) and 2(b)]. Using the yielded values of effective moments and saturated moments, we can evaluate the Rhodes-Wohlfarth ratio (RWR), which is defined as P_c/P_s, where P_c corresponds to the effective moment (μ_{eff}) as $P_c(P_c + 2) = \mu_{eff}^2$, and P_s equals the saturated moment (μ_s) [41,42]. The RWR should be 1 for a system with localized ferromagnetism, and it becomes larger than 1 in an itinerant material. In MnSb$_2$Te$_4$, the RWR is evaluated to be 2.25 and 2.22 with $H//ab$ and $H//c$, respectively, indicating an itinerant nature of the magnetism.

The susceptibility data in Fig. 1 exhibit lots of similarities when compared to previously reported ones for antiferromagnetic MnSb$_2$Te$_4$ samples [22,24], while notable differences are also detected which are particularly evident in the data for $H//c$. Actually, the magnetic properties of MnSb$_2$Te$_4$ are sensitive to the synthesis temperature. For example, the

crystals grown at 620, 630, and 640 °C exhibit various magnetic transitions at $T_N \sim 19$ K, $T_C \sim 24$ K, and $T_C \sim 34$ K [24]. Furthermore, even though the susceptibility of the MnSb$_2$Te$_4$ antiferromagnetic sample in Refs. [22] and [24] exhibits lots of similarities, notable differences also exist in the magnitude of χ and the position of H_{c2}. The χ at $T_N \sim 19$ K is about 0.88 and 2.3 emu/mol Oe for $H//c$ in Fig. 1(a) of Ref. [22] and Fig. 1(b) of Ref. [24], respectively. The $H_{c2} = 1.4$ T and $H_{c2} < 1$ T in Fig. 1(b) of Ref. [22] and Fig. 1(d) of Ref. [24], respectively. The deviation of the magnetic susceptibility data in our manuscript from Ref. [22] and Ref. [24] could be due to a minor difference of the furnace temperature induced defects or site mixing as detected by EDX.

B. Critical behavior

For a material with a second-order FM transition, the Arrott plots (a mean-field model) of M^2 versus H/M could offer an insightful understanding of the system. According to the mean-field model [43], the plots of M^2 versus H/M would exhibit a series of linear parallel lines close to T_C in the high-field region, with the curve at T_C passing through the origin point (0, 0). Furthermore, the slopes of the Arrott plots can uncover the order of the transition: A positive (negative) slope demonstrates a second-order (first-order) phase transition [44]. As displayed in Fig. 3(a), the positive slopes of the Arrott plots reveal a second-order FM transition. The curves are not parallel and nonlinear, indicating that the critical behavior of MnSb$_2$Te$_4$ cannot be well explained by the mean-field model.

Generally, the magnetic behaviors in the vicinity of T_C can be characterized by the Arrott-Noakes equation [45],

$$(H/M)^{1/\gamma} = a\varepsilon + bM^{1/\beta}, \qquad (1)$$

where γ and β denote the critical exponents, and a and b are constants. The critical exponents are defined by the following equations [46,47]:

$$M_S(T) \propto |\varepsilon|^\beta, \quad \varepsilon < 0 \text{ below } T_C, \qquad (2)$$

$$M \propto H^{1/\delta}, \quad \varepsilon = 0, T = T_C, \qquad (3)$$

$$\chi_0^{-1}(T) \propto |\varepsilon|^\gamma, \quad \varepsilon > 0 \text{ above } T_C, \qquad (4)$$

where $\varepsilon = T/T_C - 1$ represents the reduced temperature. The exponents β, δ, and γ are related to the spontaneous magnetization (M_S) below T_C, the isothermal $M(H)$ at T_C, and the inverse initial magnetic susceptibility (χ_0^{-1}) above T_C, respectively. Since the critical behavior of MnSb$_2$Te$_4$ cannot be depicted by the Arrott plot, the modified Arrott plot [$M^{1/\beta}$ versus $(H/M)^{1/\gamma}$] is employed. To acquire proper critical exponents, several universal models—the 3D Heisenberg model ($\beta = 0.365$, $\gamma = 1.386$), the tricritical mean-field model ($\beta = 0.25$, $\gamma = 1.0$), the 3D XY model ($\beta = 0.345$, $\gamma = 1.316$), the 3D Ising model ($\beta = 0.325$, $\gamma = 1.24$), and the 2D Ising model ($\beta = 0.125$, $\gamma = 1.75$)—have been opted to establish the modified Arrott plots (MAPs) [Figs. 3(b)–3(b)]. For a perfect model, the MAPs should exhibit various parallel lines. Obviously, the magnetic behavior of MnSb$_2$Te$_4$ cannot be described by the above universal models.

An iterative process is exploited to gain appropriate values of the exponents β and γ [48–50]. With an initial β and γ,
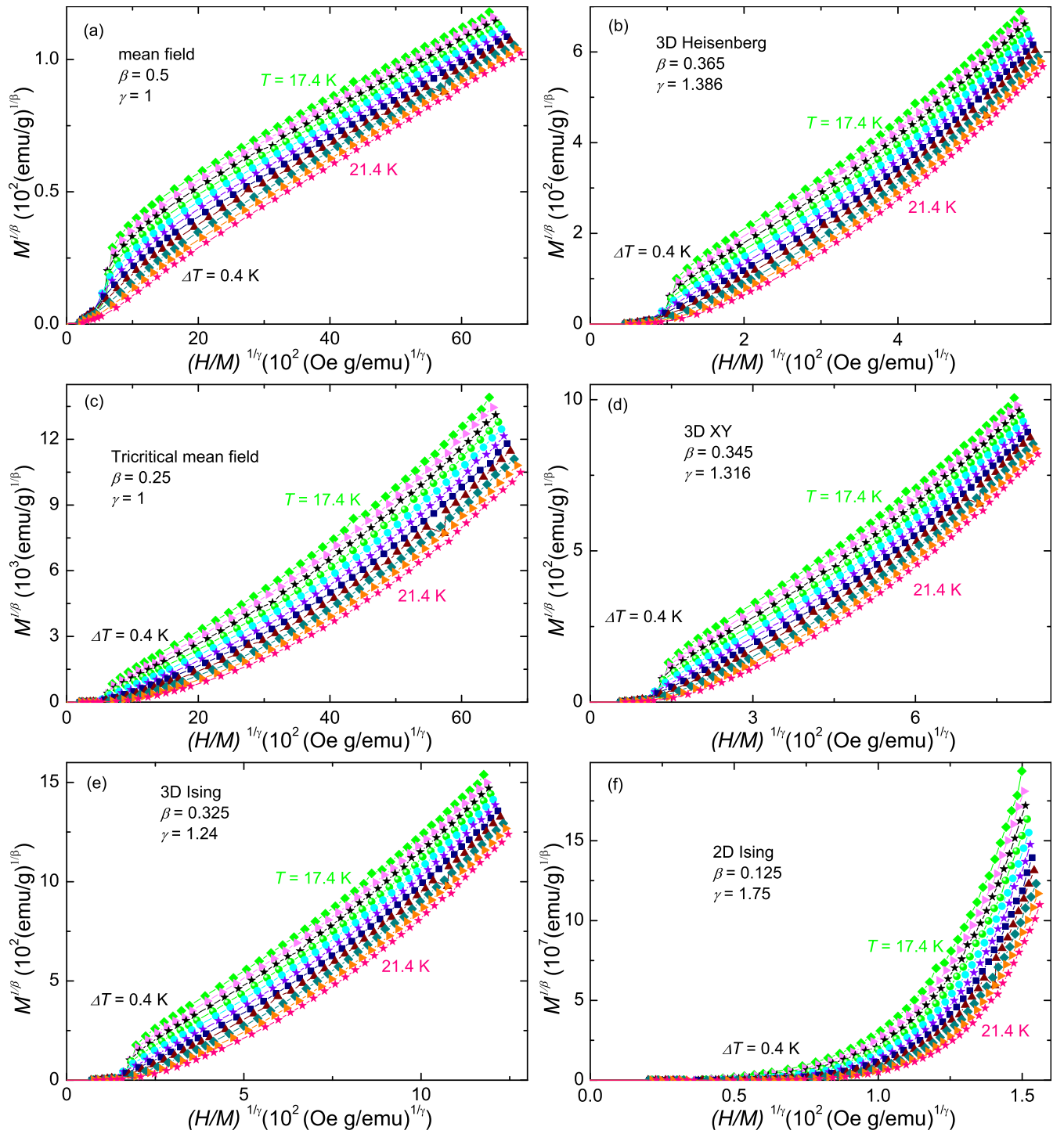
FIG. 3. Isothermal $M^{1/\beta}$ vs $(H/M)^{1/\gamma}$ curves for $H//c$ with exponents of (a) a mean-field model, (b) a 3D Heisenberg model, (c) a tricritical mean-field model, (d) a 3D XY model, (e) a 3D Ising model, and (f) a 2D Ising model.

the values of $M_S(T)$ and $\chi_0^{-1}(T)$ can be deduced by linear extrapolation from the high-field region to the intercepts of the MAPs. Using Eqs. (2) and (4), new values of β and γ are fitted, and new MAPs are constructed. The above procedures are iterated until stable values of β and γ are obtained. The critical exponents of MnSb$_2$Te$_4$ yielded by the above method are irrelevant to the initial β and γ, confirming the reliability

of the achieved exponents. The final MAPs are displayed in Fig. 4(b) with a series of straight parallel lines confirming the reliability of the obtained exponents.

The final M_S and χ_0^{-1} as a function of T are presented in Fig. 5(a). On the basis of Eqs. (2) and (4), the exponents $\beta = 0.441(9)$ with $T_C = 19.4(1)$ K and $\gamma = 1.108(13)$ with $T_C = 19.3(1)$ K are fitted with red fitting lines. Alternatively,
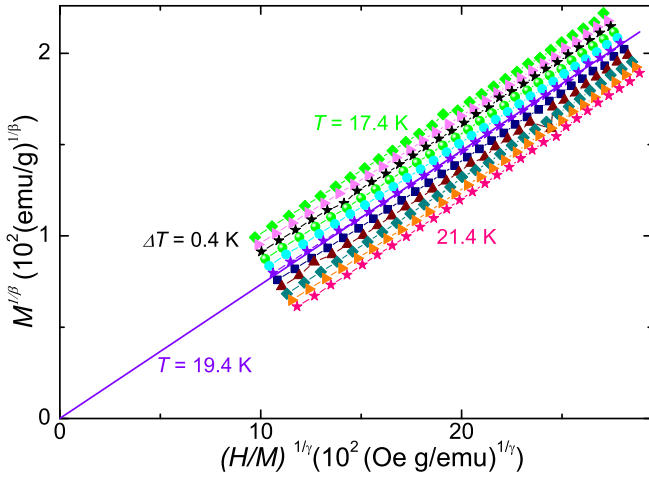
FIG. 4. The yielded modified Arrott plots of $M^{1/\beta}$ vs $(H/M)^{1/\gamma}$ with $\beta = 0.441$ and $\gamma = 1.108$.
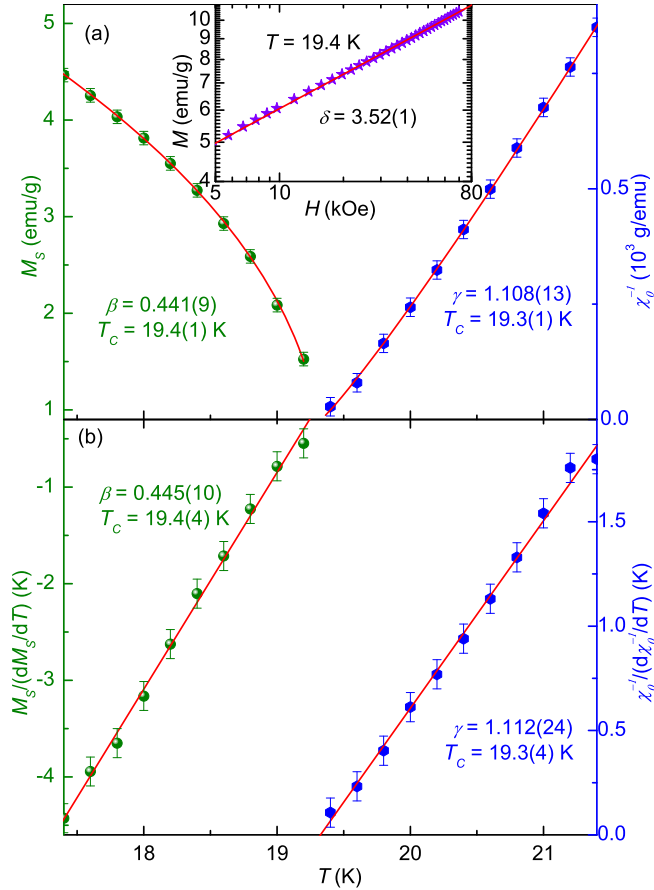

FIG. 5. (a) Fitting of the extracted final spontaneous magnetization M_S (left) and inverse initial susceptibility $1/\chi_0$ (right) from the modified Arrott plots with corresponding power laws (red lines) in Eqs. (2) and (4). Inset: An isothermal $M(H)$ at $T_C = 19.4$ K on a $\log_{10}$-$\log_{10}$ scale with a linear fitting based on Eq. (3). (b) The Kouvel-Fisher plots of $M_S(dM_S/dT)^{-1}$ (left) and $\chi_0^{-1}(d\chi_0^{-1}/dT)^{-1}$ (right) as a function of temperature, with the linear fitting line based on Eqs. (5) and (6).

the generated exponents can be checked by the Kouvel-Fisher (KF) technique [51],

$$\frac{M_S(T)}{dM_S(T)/dT} = \frac{T - T_C}{\beta}, \tag{5}$$

$$\frac{\chi_0^{-1}(T)}{d\chi_0^{-1}(T)/dT} = \frac{T - T_C}{\gamma}. \tag{6}$$

As presented in Fig. 5(b), the linear fitting of $M_S/(dM_S/dT)$ and $\chi_0^{-1}/(d\chi_0^{-1}/dT)$ versus T yields $\beta = 0.445(10)$ with $T_C = 19.4(4)$ K and $\gamma = 1.112(24)$ with $T_C = 19.3(4)$ K, consistent with the values from the MAPs. The inset of Fig. 5(a) displays the $M(H)$ at $T_C \sim 19.4$ K on a $\log_{10}$-$\log_{10}$ scale. The third critical exponent $\delta = 3.52(1)$ is fitted by Eq. (4). The reliability of the above generated exponents can be examined by the Widom relation [52],

$$\delta = 1 + \gamma/\beta. \tag{7}$$

Utilizing β and γ from the MAPs and the KF method, $\delta = 3.51(8)$ and $3.50(11)$ can be calculated, respectively. These calculated values are quite close to the direct fitted value by the critical isotherm within the experimental error, verifying the self-consistency of the yielded critical exponents.

As the temperature range selected for the above critical behavior analysis of $|\varepsilon| = |T - T_C|/T_C \leqslant 0.1$ is larger than the typical asymptotic critical region of $|\varepsilon| = |T - T_C|/T_C \leqslant 0.01$, it is worthwhile to check the exponents in the asymptotic critical region. Thus the effective exponents β_{eff} and γ_{eff} are generated as [53]

$$\beta_{\text{eff}} = \frac{d[\ln M_S(\varepsilon)]}{d(\ln \varepsilon)}, \quad \gamma_{\text{eff}} = \frac{d[\ln \chi_0^{-1}(\varepsilon)]}{d(\ln \varepsilon)}. \tag{8}$$

The obtained effective exponents β_{eff} and γ_{eff} as a function of the reduced temperature $|\varepsilon|$ are presented in Fig. 6. In the asymptotic critical region, we acquire $\beta_{\text{eff}} = 0.434$ at $|\varepsilon|_{\min} = 0.008$ and $\gamma_{\text{eff}} = 1.096$ at $|\varepsilon|_{\min} = 0.004$, which are approaching the $\beta = 0.441$ and $\gamma = 1.108$ obtained by MAPs, demonstrating that the obtained critical exponents in Fig. 5 are close to the asymptotic critical exponents.

The accuracy of the yielded exponents can be further examined by scaling processes. For proper critical exponents of β and γ, the magnetic equation of state in the asymptotic critical region should fulfill the following scaling function [52]:

$$M(H, \varepsilon) = \varepsilon^{\beta} f_{\pm}(H/\varepsilon^{\beta+\gamma}), \tag{9}$$

where $f_-(T < T_C)$ and $f_+(T > T_C)$ represent regular functions. In terms of scaled magnetization $m = M|\varepsilon|^{-\beta}$ and scaled field $h = H|\varepsilon|^{-(\beta+\gamma)}$, Eq. (9) can be stated as $m = f_{\pm}(h)$. The equation indicates that for appropriate selected critical exponents, the plots of renormalized $m(h)$ should collapse onto two distinct branches below T_C and above T_C. Figure 7 displays $m(h)$ curves in the high-field region, which indeed split into two separate branches. Furthermore, the scaling magnetic equation of state can take the following form [46]:

$$\frac{M}{H^{\delta}} = h\left(\frac{\varepsilon}{H^{1/\beta}}\right), \tag{10}$$

where h is a scaling function. If proper values of β, γ, δ, and T_C are achieved, the scaling plots should collapse onto a
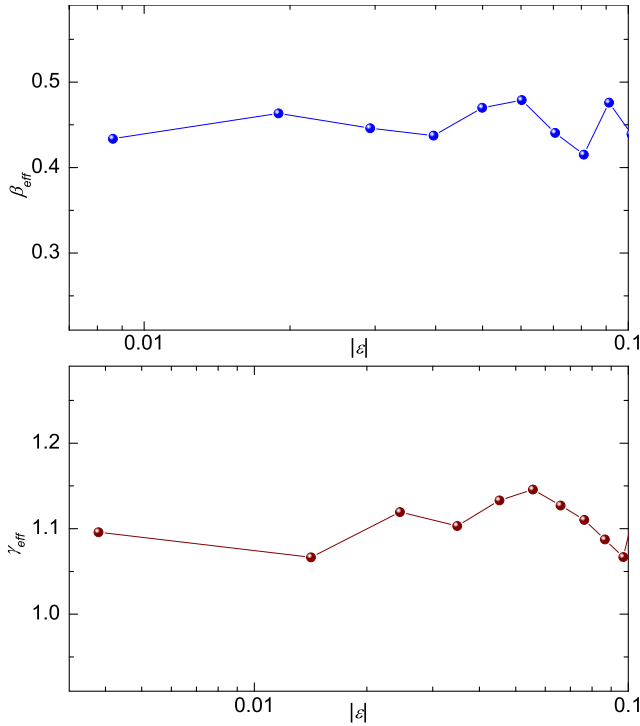
FIG. 6. The effective exponents β_{eff} and γ_{eff} as a function of the reduced temperature $|\varepsilon|$.

FIG. 8. Plots of m^2 vs h/m below T_C in the low-field region on a $\log_{10}$-$\log_{10}$ scale. Inset: The H-T phase graph of $MnSb_2Te_4$ (AFM, CAFM, and FM refer to the antiferromagnetic, canted antiferromagnetic, and ferromagnetic phases). The corresponding arrows represent the magnetic order formed by the Mn FM layers, showing AFM, CAFM, and FM orders, respectively.

universal curve. Using the deduced critical exponents from the MAPs method, the scaled data of $MH^{-1/\delta}$ versus $\varepsilon H^{-1/(\beta\delta)}$ in the high-field region are plotted in the inset of Fig. 7, exhibiting excellent overlap of the curves. The above scaling processes further assure the reliability and accuracy of the generated critical exponents and T_C.

Then, we concentrate on the scaling in the low-field region. As field-induced phase transitions occur in low field, inflection points occur in the isothermal $M(H)$ curve, resulting in divergent scaling curves [27,54]. Figure 8 displayed the
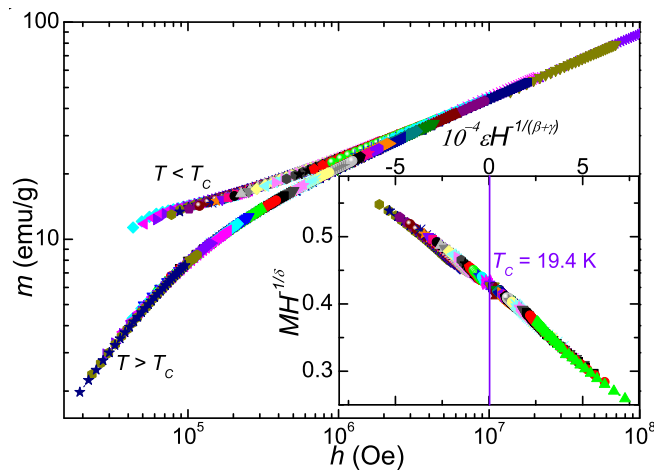

FIG. 7. Scaling plots of renormalized magnetization $m = M|\varepsilon|^{-\beta}$ vs renormalized field $h = H|\varepsilon|^{-(\beta+\gamma)}$ in the high-field region on a $\log_{10}$-$\log_{10}$ scale. Inset: Scaling $M(H)$ curves by $MH^{-1/\delta}$ vs $\varepsilon H^{-1/(\beta\delta)}$.
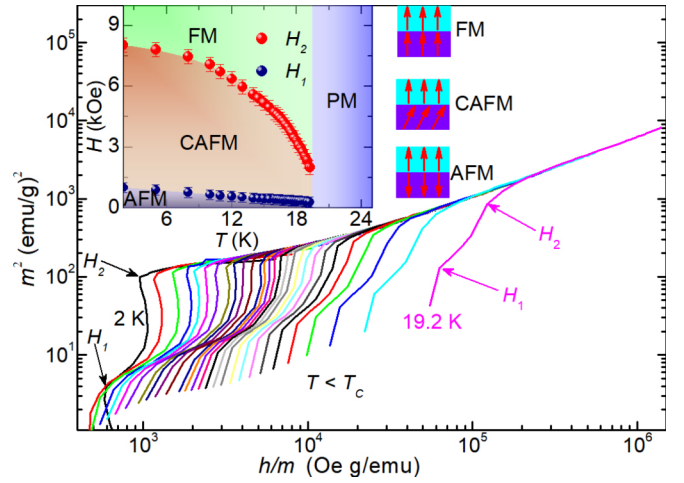
scaling m^2 versus h/m curves in the low-field region, where two turning points are present in each curve. The inflection points of the isothermal field-dependent $M(H)$ curves in the inset of Fig. 1(b) and the following deduced isothermal ΔS_M curves in Fig. 10 are consistent with the determined points of H_1 and H_2 in Fig. 8 within the experimental error range. Taking into account the inflection points in isothermal M versus H [Fig. 1(b)], m^2 versus h/m (Fig. 8), and ΔS_M versus H (Fig. 10) curves, the phase diagram with the error bar is constructed (inset of Fig. 8), in which the boundaries of the AFM, the CAFM, and the FM states can be clearly determined. With an increase of the applied external field, the AFM phase is modulated to the CAFM state at H_1 and subsequently polarized into the FM state when $H > H_2$. In the phase diagram, two triple points are discovered. One is located at the intersection across the AFM, the CAFM, and the PM phases ($\sim$310 Oe at 19.4 K); the other on the boundaries of the CAFM, the FM, and the PM states ($\sim$1970 Oe at 19.4 K).

In Table I, we summarize the critical exponents estimated from various approaches, as well as the anticipated values for different theoretical models. The critical exponent β of a two-dimensional (2D) ferromagnetic system should be in a window $\sim 0.1 \leqslant \beta \leqslant 0.25$ [57]. The extracted value of β reveals a 3D critical behavior in $MnSb_2Te_4$. The critical exponents cannot be characterized by any single theoretical models, i.e., β is between the 3D-Heisenberg model and the mean-field model, and γ is between the 3D-Ising model and the mean-field model, indicating complex magnetic interactions in $MnSb_2Te_4$ [27]. The universal classes of the FM transition are decided by the exchange interaction $J(r)$. On the basis of the renormalization-group theory [58,59], the exchange interaction $J(r)$ decays with spatial distance r as $J(r) \sim r^{-(d+\sigma)}$ for long-range interaction, where d represents spatial dimensionality and σ is a positive constant correlated with the range of the interaction. Furthermore, the $J(r)$ is

TABLE I. Comparison of the extracted values of critical exponents of $MnSb_2Te_4$ with various theoretical universal models [the modified Arrott plot (MAP), the Kouvel-Fisher plot (KFP), the critical isotherm (CI), the magnetic entropy change (MEC), and cal = calculated].

Composition	Ref.	Technique	β	γ	δ	n	m
$MnSb_2Te_4$ S1	This work	MAP	0.441(9)	1.108(13)	3.51(8)^{cal}		
	This work	KFP	0.445(10)	1.112(24)	3.50(11)^{cal}		
	This work	CI			3.52(1)		
	This work	MEC				0.727(7)	1.184(10)
$MnSb_2Te_4$ S2	This work	MAP	0.575(8)	0.876(4)	2.52(4)^{cal}		
3D XY	[55]	Theory	0.345	1.316	4.81	0.606	1.208
3D Heisenberg	[55]	Theory	0.365	1.386	4.8	0.637	1.208
3D Ising	[55]	Theory	0.325	1.24	4.82	0.569	1.207
2D Ising	[56]	Theory	0.125	1.75	15	0.533	1.06
Tricritical mean field	[55]	Theory	0.25	1.0	5	0.4	1.20
Mean field	[55]	Theory	0.5	1.0	3.0	0.667	1.333

connected with σ and γ as

$$\gamma = 1 + \frac{4}{d}\frac{(n+2)}{(n+8)}\Delta\sigma + \frac{8(n+2)(n-4)}{d^2(n+8)^2}$$
$$\times \left[1 + \frac{2G\left(\frac{d}{2}\right)(7n+20)}{(n-4)(n+8)}\right]\Delta\sigma^2, \qquad (11)$$

where $G\left(\frac{d}{2}\right) = 3 - \frac{1}{4}\left(\frac{d}{2}\right)^2$, $\Delta\sigma = \sigma - d/2$, and n is the spin dimensionality. When $\sigma > 2$, the 3D Heisenberg model with a short-range magnetic interaction is valid, and $J(r)$ decays faster than r^{-5}. When $\sigma < 3/2$, the mean-field model with a long-range magnetic interaction is effective, where $J(r)$ decays slower than $r^{-4.5}$. The parameters in Eq. (11) are adjusted for particular values of $\{d : n\}$ to generate values consistent with those that are experimentally obtained. The process is repeated with different sets of $\{d : n\}$. It is found that $\{d : n\} = \{3 : 2\}$ and $\sigma = 1.67$ give the exponents ($\beta = 0.439$, $\gamma = 1.108$, and $\delta = 3.52$), which are mostly close to our experimentally acquired values (Table I). In addition, we obtain the correlation length critical exponent $\nu = 0.664$ [$\nu = \gamma/\sigma$, $\xi = \xi_0|(T - T_C)/T_C|^{-\nu}$], and $\alpha = 0.008$ ($\alpha = 2 - \nu d$). This calculation suggests a complex magnetic exchange between a long-range and short-range magnetic interaction with exchange interaction decays as $r^{-4.67}$.

We now discuss our observations by the Stoner-Wohlfarth model and SCR theory, which are theories applicable for itinerant ferromagnets. The Stoner-Wohlfarth model is suitable for very weak itinerant-electron ferromagnetic systems [60,61], which always show parallel isothermal lines in the plot of M^2 versus H/M (the mean-field model) for both paramagnetically and ferromagnetically ordered phases. The curvature in Fig. 3(a) excluded $MnSb_2Te_4$ as a very weak itinerant-electron ferromagnet, which is consistent with the calculated RWR value of 2.25 (2.22) for $H//ab$ ($H//c$). In SCR theory [62,63], M^4 should obey the linear relation against H/M, as $M^4 = 1.17 \times 10^{18} (T_C^2/T_A^3)H/M$, i.e., the tricritical mean-field model should consist of linear lines, which are not observed in Fig. 3(c), indicating that the SCR theory is not a proper model for $MnSb_2Te_4$. The observed deviation from any existing models demonstrates complex magnetic interactions in $MnSb_2Te_4$ that cannot be simply explained by the long-range weak itinerant mean-field model, the itinerant

tricritical mean-field model, or even the short-range localized 3D Heisenberg model, consistent with the results from the renormalization-group theory.

To check how the critical exponents depend on samples, we fabricated another $MnSb_2Te_4$ sample S2, which is decanted at 886 K. The $M(T)$ and $M(H)$ curves in Fig. 1 exhibit notable differences with the sample S2 in Fig. S1 in the Supplemental Material [64]. The critical behavior is then analyzed by MAPs as shown in Fig. S2 in the Supplemental Material [64]. On the basis of Eqs. (2) and (4), the exponents $\beta = 0.575(8)$ with $T_C = 21.4(1)$ K and $\gamma = 0.876(4)$ with $T_C = 21.4(1)$ K are fitted with red fitting lines as displayed in Fig. S3 in the Supplemental Material [64]. The yielded critical exponents of sample S2 are summarized in Table I, which exhibit substantial differences with sample S1. The results imply that the estimates of critical exponents are affected by sample-dependent variables, further indicating complex magnetic interactions in $MnSb_2Te_4$. Further efforts to tune the magnetic properties by fabricating various samples and to measure the critical behaviors are underway.

C. Magnetic entropy change

Exploiting Maxwell's relation and thermodynamic theory, the magnetic entropy change $\Delta S_M(T, H)$ can be evaluated as [65,66]

$$\Delta S_M(T, H) = \mu_0 \int_0^H \left(\frac{\partial M}{\partial T}\right)_H dH. \qquad (12)$$

The calculated ΔS_M as a function a temperature under a series of fields up to 70 kOe in $H//ab$ and $H//c$ are displayed in Figs. 9(a) and 9(b), respectively. The curves show broad peaks around T_C in the high-field region, exhibiting typical FM behavior. The maximum values of ΔS_M at 70 kOe are 2.20 J kg^{-1} K^{-1} in the ab plane and 2.20 J kg^{-1} K^{-1} along the c axis. The values of ΔS_M^{max} are comparable with common low-dimensional second-order FM materials, such as 2.5 J kg^{-1} K^{-1} in $Mn_3Si_2Te_6$ [67], 1.7 J kg^{-1} K^{-1} in 2H-$Mn_{0.28}TaS_2$ [31], and 3.28 J kg^{-1} K^{-1} in $AlCMn_3$ [68]. Furthermore, the temperature- and field-dependent rotating magnetic entropy change $\Delta S_M^R(T, H) = [\Delta S_M(T, H_{ab})] -$
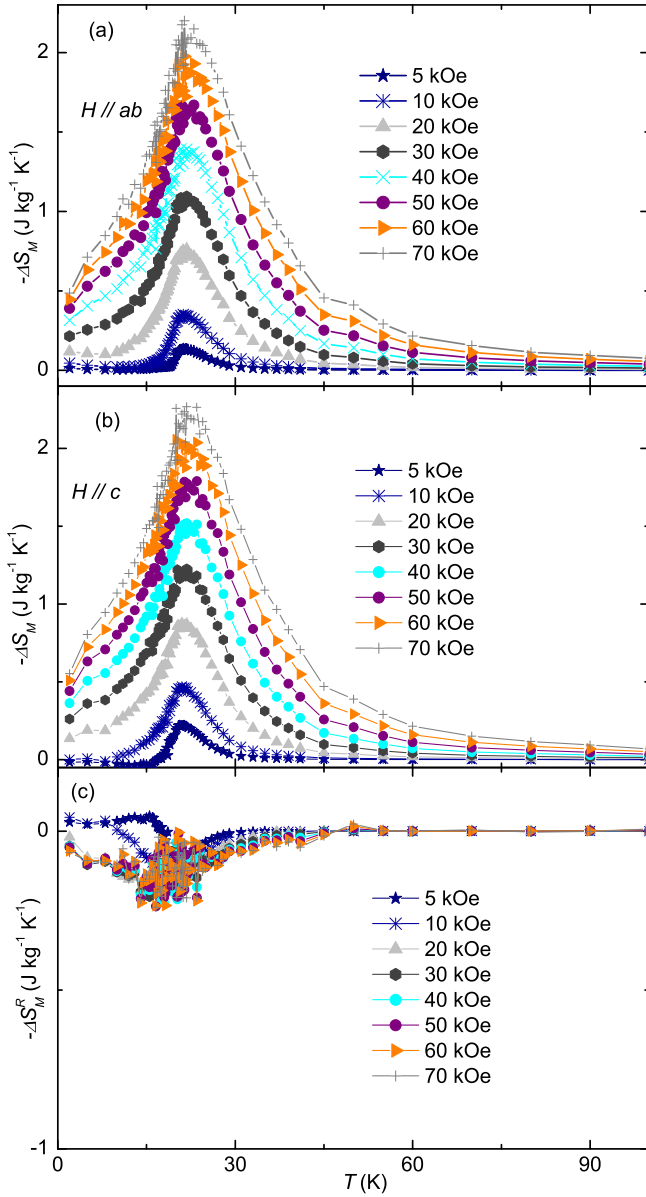
FIG. 9. (a),(b) Temperature-dependent magnetic entropy change $[\Delta S_M(T,H)]$ of MnSb$_2$Te$_4$ under various fields applied along (a) $H//ab$ and (b) $H//c$. (c) The rotating magnetic entropy change $[\Delta S_M^R(T,H) = \Delta S_M(T,H_{ab}) - \Delta S_M(T,H_c)]$ vs T.

$[\Delta S_M(T,H_c)]$ is calculated. As shown in Fig. 9(c), $-\Delta S_M^R$ is ~ 0 J kg^{-1} K^{-1} at $T > 39$ K, displaying a nearly isotropic behavior well above T_C, consistent with the above Curie-Weiss fitting; and $-\Delta S_M^R$ is less than 0.24 J kg^{-1} K^{-1} at low temperature, demonstrating weak anisotropy. Additionally, the field-dependent isothermal ΔS_M at various temperatures below T_C is also generated and presented in Fig. 10, where the anomalies from AFM-CAFM and CAFM-FM transitions are prominent, and the deduced $H_1 = 1.0$ kOe and $H_2 = 8.0$ kOe at $T = 2$ K from the enlarged ΔS_M versus H curve (inset of Fig. 10) are consistent with the obtained values from plots of m^2 versus h/m (Fig. 8), further confirming the reliability of the phase diagram in the inset of Fig. 8.
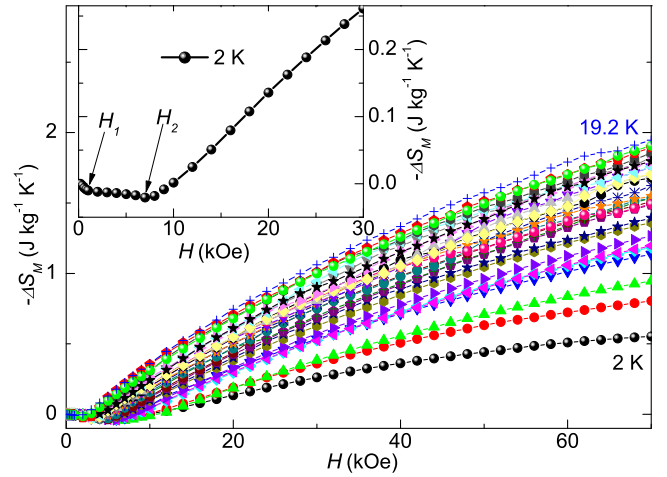

FIG. 10. Field dependence of isothermal ΔS_M at various temperatures below T_C. Inset: Enlarged plot of ΔS_M vs H at $T = 2$ K.

For materials with a second-order FM transition, the maximum of the magnetic entropy change $-\Delta S_M^{\max}$ and relative cooling power (RCP) versus H should display power-law behaviors [69–71],

$$-\Delta S_M^{\max} \propto H^n, \tag{13}$$

$$\text{RCP} \propto H^m, \tag{14}$$

where RCP is defined as the product of $-\Delta S_M^{\max}$ and the full width at half-maximum δ_{FWHM}, and n and m can be related to the critical exponents β, γ, and δ as [70,71]

$$n(T_C) = 1 + (\beta - 1)/(\beta + \gamma), \tag{15}$$

$$m = 1 + 1/\delta. \tag{16}$$

The field dependence of $-\Delta S_M^{\max}$ and RCP are displayed on the left and right axes of Fig. 11, respectively. In the high-field FM region ($H > 30$ kOe), the plots obey well the power-law fitting, which gives $n = 0.727(7)$ and $m = 1.184(10)$. In the
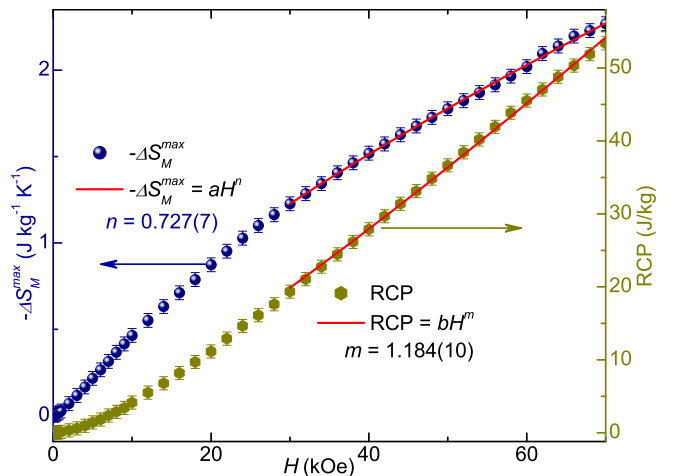

FIG. 11. The maximum of the magnetic entropy change $\Delta S_M^{\max}$ and the relative cooling power RCP of MnSb$_2$Te$_4$ as a function of temperature for $H//c$.

low-field region, the curves deviate from the power law, which is consistent with the presence of an AFM state. The power-law behaviors are suitable for systems with a second-order FM transition in the high-field FM region.

Utilizing the exponents by MAP summarized in Table I, the exponents can be calculated as $n = 0.639$ (15) and $m = 1.285$ (29) according to Eqs. (15) and (16), which exhibit substantial differences with the values of n and m deduced by the above power-law fitting. The discrepancy is rather common in magnetic systems, such as $CrSbSe_3$ [72], $Fe_{3−x}GeTe_2$ [73], CrI_3 [74], and VI_3 [75]. The origin is still controversial, possibly because of the different fitting regions [75]. Actually, using a smaller fitting range of $40 < H < 60$ kOe, $n = 0.685(3)$ and $m = 1.203(4)$ can be fitted; the values approach those obtained by the MAP.

For systems with a second-order FM transition, the curves of $\Delta S_M(T, H)$ can be normalized into a single universal curve [71] when plotted as the reduced magnetic entropy change $(\Delta S_M / \Delta S_M^{\max})$ versus a scaled temperature θ defined as [76]

$$\theta_- = (T_C - T)/(T_{r1} - T_C), \quad T < T_C, \quad (17)$$

$$\theta_+ = (T - T_C)/(T_{r2} - T_C), \quad T > T_C, \quad (18)$$

where T_{r1} and T_{r2} [the inset of Fig. 12(a)] represent the temperatures that refer to the full width at half-maximum $\Delta S_M(T_{r1}, T_{r2}) = \frac{1}{2} \Delta S_M^{\max}$. Figure 12(a) indicates that all the $\Delta S_M(T, H)$ curves fall into a single universal master curve in the high-field FM region, indicating a second-order phase transition. Moreover, ΔS_M can also be scaled as the following equation [77]:

$$-\Delta S_M \propto H^n F\left(\frac{\varepsilon}{H^{1/(\beta+\gamma)}}\right), \quad (19)$$

where F represents a regular scaling function, and β, γ, and n are critical exponents. As displayed in Fig. 12(b), all the plots of $\frac{-\Delta S_M(T)}{H^n}$ versus $\frac{\varepsilon}{H^{1/(\beta+\gamma)}}$ collapse onto a single universal curve in the high-field FM region, further verifying the reliability and accuracy of the acquired critical exponents. As the scaling law is only valid in a second-order FM state, the well normalized curves in the high-field region verify the existence of the FM state, and the deviation in low field is consistent with the presence of AFM and CAFM states.

For the in-depth investigation and further modulation of nontrivial topological properties in $MnSb_2Te_4$, exploration of the magnetic structure and magnetic interactions is crucial. As we know, spin-orbital coupling and magnetic interaction is essential in the formation and evolution of topological states [78,79]. In $MnBi_2Te_4$, an axion state presents at the AFM ground state, and a minimal ideal Weyl semimetal is preferred at the spin-polarized FM state [9,19]. In NdSb, a Dirac semimetal is at the AFM ground state, which evolves to a Weyl semimetal at the FM state [80,81]. In PrAlGe, the FM order leads to the presence of band splitting and induces a shift of Weyl nodes to break time-reversal symmetry [78,82]. A comprehensive analysis of the critical behavior and construction of the phase diagram, which explicitly describes the relations between temperature, field, and magnetic
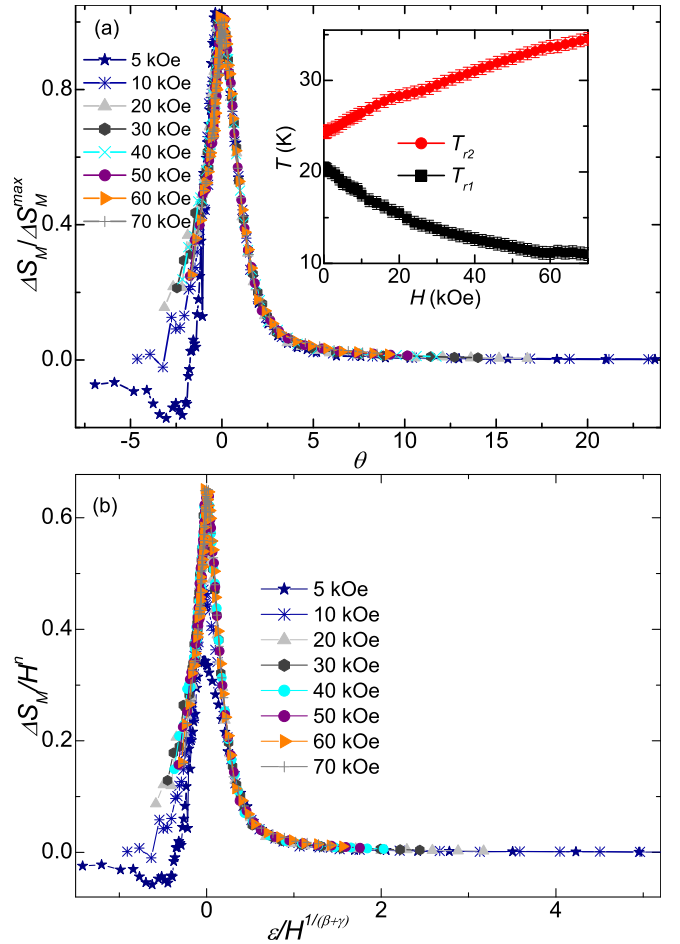

FIG. 12. (a) The renormalized magnetic entropy change $\Delta S_M / \Delta S_M^{\max}$ as a function of the scaled temperature θ. Inset: The reference temperatures T_{r1} and T_{r2} vs field H. (b) Scaling $\Delta S_M(T, H)$ under the yielded exponents.

order, is essential for clarification of the topological nature of $MnSb_2Te_4$.

IV. CONCLUSIONS

In conclusion, the magnetic properties, critical behaviors, and magnetic entropy change of $MnSb_2Te_4$ single crystals have been comprehensively explored. The $M(T)$ reveals an anisotropic magnetic order with the c axis as the easy axis at low temperature and an almost isotropic magnetic behavior at high temperature. The yielded RWR verifies an itinerant ferromagnetism in high field. By critical-behavior analysis in the vicinity of the PM-FM transition, the critical exponents β, γ, and δ are deduced, exhibiting a 3D critical behavior and complicated magnetic interactions. The obtained $J(r) \sim r^{-4.67}$ suggests that the magnetic interaction lies between a long-range and short-range magnetic interaction. Two triple points at a temperature and field of ∼310 Oe at 19.4 K and ∼1970 Oe at 19.4 K are determined. Moreover, a nearly isotropic behavior well above T_C and weak anisotropic features at low temperature are further confirmed in magnetic entropy change. The field-dependent $-\Delta S_M^{\max}$ and RCP follow the power-law behavior. The scaling analyses on $-\Delta S_M$ verify a high-field second-order FM order.

[1] L. Ye, M. Kang, J. Liu, F. von Cube, C. R. Wicker, T. Suzuki, C. Jozwiak, A. Bostwick, E. Rotenberg, D. C. Bell, L. Fu, R. Comin, and J. G. Checkelsky, Nature (London) **555**, 638 (2018).

[2] N. Morali, R. Batabyal, P. K. Nag, E. Liu, Q. Xu, Y. Sun, B. Yan, C. Felser, N. Avraham, and H. Beidenkopf, Science **365**, 1286 (2019).

[3] Y. J. Chen, L. X. Xu, J. H. Li, Y. W. Li, H. Y. Wang, C. F. Zhang, H. Li, Y. Wu, A. J. Liang, C. Chen, S. W. Jung, C. Cacho, Y. H. Mao, S. Liu, M. X. Wang, Y. F. Guo, Y. Xu, Z. K. Liu, L. X. Yang, and Y. L. Chen, Phys. Rev. X **9**, 041040 (2019).

[4] D. Nevola, H. X. Li, J.-Q. Yan, R. G. Moore, H.-N. Lee, H. Miao, and P. D. Johnson, Phys. Rev. Lett. **125**, 117205 (2020).

[5] A. K. Nayak, J. E. Fischer, Y. Sun, B. Yan, J. Karel, A. C. Komarek, C. Shekhar, N. Kumar, W. Schnelle, J. Kubler, C. Felser, and S. S. P. Parkin, Sci. Adv. **2**, e1501870 (2016).

[6] S. Nakatsuji, N. Kiyohara, and T. Higo, Nature (London) **527**, 212 (2015).

[7] M. Ikhlas, T. Tomita, T. Koretsune, M.-T. Suzuki, D. Nishio-Hamane, R. Arita, Y. Otani, and S. Nakatsuji, Nat. Phys. **13**, 1085 (2017).

[8] C. Liu, Y. Wang, H. Li, Y. Wu, Y. Li, J. Li, K. He, Y. Xu, J. Zhang, and Y. Wang, Nat. Mater. **19**, 522 (2020).

[9] D. Q. Zhang, M. J. Shi, T. S. Zhu, D. Y. Xing, H. J. Zhang, and J. Wang, Phys. Rev. Lett. **122**, 206401 (2019).

[10] M. M. Otrokov, I. P. Rusinov, M. Blanco-Rey, M. Hoffmann, A. Y. Vyazovskaya, S. V. Eremeev, A. Ernst, P. M. Echenique, A. Arnau, and E. V. Chulkov, Phys. Rev. Lett. **122**, 107202 (2019).

[11] H. Li, S. Y. Gao, S. F. Duan, Y. F. Xu, K. J. Zhu, S. J. Tian, J. C. Gao, W. H. Fan, Z. C. Rao, J. R. Huang, J. J. Li, D. Y. Yan, Z. T. Liu, W. L. Liu, Y. B. Huang, Y. L. Li, Y. Liu, G. B. Zhang, P. Zhang, T. Kondo *et al.*, Phys. Rev. X **9**, 041039 (2019).

[12] H. Li, W. Gao, Z. Chen, W. Chu, Y. Nie, S. Ma, Y. Han, M. Wu, T. Li, Q. Niu, W. Ning, X. Zhu, and M. Tian, Phys. Rev. B **104**, 054435 (2021).

[13] Z. Liang, A. Luo, M. Shi, Q. Zhang, S. Nie, J. J. Ying, J. F. He, T. Wu, Z. Wang, G. Xu, Z. Wang, and X. H. Chen, Phys. Rev. B **102**, 161115(R) (2020).

[14] Y. J. Hao, P. Liu, Y. Feng, X. M. Ma, E. F. Schwier, M. Arita, S. Kumar, C. Hu, R. Lu, M. Zeng, Y. Wang, Z. Hao, H. Y. Sun, K. Zhang, J. Mei, N. Ni, L. Wu, K. Shimada, C. Chen, Q. Liu, and C. Liu, Phys. Rev. X **9**, 041038 (2019).

[15] B. Lian, Z. C. Liu, Y. Zhang, and J. Wang, Phys. Rev. Lett. **124**, 126402 (2020).

[16] M. M. Otrokov, I. I. Klimovskikh, H. Bentmann, D. Estyunin, A. Zeugner, Z. S. Aliev, S. Gaß, A. U. B. Wolter, A. V. Koroleva, A. M. Shikin, M. Blanco-Rey, M. Hoffmann, I. P. Rusinov, A. Yu. Vyazovskaya, S. V. Eremeev, Yu. M. Koroteev, V. M. Kuznetsov, F. Freyse, J. Sánchez-Barriga, I. R. Amiraslanov *et al.*, Nature (London) **576**, 416 (2019).

[17] Y. Deng, Y. Yu, M. Z. Shi, Z. Guo, Z. Xu, J. Wang, X. H. Chen, and Y. Zhang, Science **367**, 895 (2020).

[18] C. Hu, L. Ding, K. N. Gordon, B. Ghosh, H. Tien, H. Li, A. G. Linn, S. Lien, C.-Y. Huang, S. Mackey, J. Liu, P. V. S. Reddy, B. Singh, A. Agarwal, A. Bansil, M. Song, D. Li, S.-Y. Xu, H. Lin, H. Cao T.-R. Chang, D. Dessau, and N. Ni, Sci. Adv. **6**, eaba4275 (2020).

[19] J. Li, C. Wang, Z. Zhang, B. L. Gu, W. Duan, and Y. Xu, Phys. Rev. B **100**, 121103(R) (2019).

[20] L. Q. Zhou, Z. Y. Tan, D. Y. Yan, Z. Fang, Y. G. Shi, and H. M. Weng, Phys. Rev. B **102**, 085114 (2020).

[21] T. Murakami, Y. Nambu, T. Koretsune, G. Xiangyu, T. Yamamoto, C. M. Brown, and H. Kageyama, Phys. Rev. B **100**, 195103 (2019).

[22] S. Huan, D. Wang, H. Su, H. Wang, X. Wang, N. Yu, Z. Zou, H. Zhang, and Y. Guo, Appl. Phys. Lett. **118**, 192105 (2021).

[23] W. Ge, P. M. Sass, J. Yan, S. H. Lee, Z. Mao, and W. Wu, Phys. Rev. B **103**, 134403 (2021).

[24] Y. Liu, L. L. Wang, Q. Zheng, Z. Huang, X. Wang, M. Chi, Y. Wu, B. C. Chakoumakos, M. A. McGuire, B. C. Sales, W. Wu, and J. Yan, Phys. Rev. X **11**, 021033 (2021).

[25] J. Cui, M. Shi, H. Wang, F. Yu, T. Wu, X. Luo, J. Ying, and X. Chen, Phys. Rev. B **99**, 155125 (2019).

[26] M. Z. Shi, B. Lei, C. S. Zhu, D. H. Ma, J. H. Cui, Z. L. Sun, J. J. Ying, and X. H. Chen, Phys. Rev. B **100**, 155144 (2019).

[27] A. Wang, A. Rahman, Z. Du, J. Zhao, F. Meng, W. Liu, J. Fan, C. Ma, M. Ge, L. Pi, L. Zhang, and Y. Zhang, Phys. Rev. B **108**, 094429 (2023).

[28] X. Yang, J. Pan, X. He, L. Cao, Y. Cao, and Y. Tao, Phys. Rev. B **107**, 054440 (2023).

[29] M. E. Fisher, Rev. Mod. Phys. **46**, 597 (1974).

[30] H. E. Stanley, Rev. Mod. Phys. **71**, S358 (1999).

[31] Y. Liu, Z. Hu, E. Stavitski, K. Attenkofer, and C. Petrovic, Phys. Rev. B **103**, 144432 (2021).

[32] Y. Liu, Z. Hu, E. Stavitski, K. Attenkofer, and C. Petrovic, Phys. Rev. Res. **3**, 023181 (2021).

[33] S. Huan, S. Zhang, Z. Jiang, H. Su, H. Wang, X. Zhang, Y. Yang, Z. Liu, X. Wang, N. Yu, Z. Zou, D. Shen, J. Liu, and Y. Guo, Phys. Rev. Lett. **126**, 246601 (2021).

[34] S. H. Lee, Y. Zhu, Y. Wang, L. Miao, T. Pillsbury, H. Yi, S. Kempinger, J. Hu, C. A. Heikes, P. Quarterman, W. Ratcliff, J. A. Borchers, H. Zhang, X. Ke, D. Graf, N. Alem, C.-Z. Chang, N. Samarth, and Z. Mao, Phys. Rev. Res. **1**, 012011(R) (2019).

[35] J. Blawat, M. Marshall, J. Singleton, E. Feng, H. Cao, W. Xie, and R. Jin, Adv. Quantum Technol. **5**, 2200012 (2022).

[36] Y. Zhang, K. Deng, X. Zhang, M. Wang, Y. Wang, C. Liu, J.-W. Mei, S. Kumar, E. F. Schwier, K. Shimada, C. Chen, and B. Shen, Phys. Rev. B **101**, 205126 (2020).

[37] J. Q. Yan, Q. Zhang, T. Heitmann, Z. Huang, K. Y. Chen, J. G. Cheng, W. Wu, D. Vaknin, B. C. Sales, and R. J. McQueeney, Phys. Rev. Mater. **3**, 064202 (2019).

[38] B. Chen, F. Fei, D. Zhang, B. Zhang, W. Liu, S. Zhang, P. Wang, B. Wei, Y. Zhang, Z. Zuo, J. Guo, Q. Liu, Z. Wang, X. Wu, J. Zong, X. Xie, W. Chen, Z. Sun, S. Wang, Y. Zhang, M. Zhang, X. Wang, F. Song, H. Zhang, D. Shen, and B. Wang, Nat. Commun. **10**, 4469 (2019).

[39] H. Li, S. Liu, C. Liu, J. Zhang, Y. Xu, R. Yu, Y. Wu, Y. Zhang, and S. Fan, Phys. Chem. Chem. Phys. **22**, 556 (2020).

[40] J. Q. Yan, S. Okamoto, M. A. McGuire, A. F. May, R. J. McQueeney, and B. C. Sales, Phys. Rev. B **100**, 104409 (2019).

[41] E. P. Wohlfarth, J. Magn. Magn. Mater. **7**, 113 (1978).

[42] T. Moriya, J. Magn. Magn. Mater. **14**, 1 (1979).

[43] A. Arrott, Phys. Rev. **108**, 1394 (1957).

[44] S. K. Banerjee, Phys. Lett. **12**, 16 (1964).

[45] A. Arrott and J. Noakes, Phys. Rev. Lett. **19**, 786 (1967).

[46] H. E. Stanley, *Introduction to Phase Transitions and Critical Phenomena* (Oxford University Press, London, 1971).

[47] M. E. Fisher, Rep. Prog. Phys. **30**, 615 (1967).

[48] A. K. Pramanik and A. Banerjee, Phys. Rev. B **79**, 214426 (2009).

[49] X. Yang, J. Pan, S. Liu, M. Yang, L. Cao, D. Chu, and K. Sun, Phys. Rev. B **103**, 104405 (2021).

[50] X. Yang, J. Pan, K. Sun, Y. Shi, L. Cao, S. Liu, W. Gai, D. Chu, and M. Yang, J. Alloys Compd. **886**, 161118 (2021).

[51] J. S. Kouvel and M. E. Fisher, Phys. Rev. **136**, A1626 (1964).

[52] B. Widom, J. Chem. Phys. **43**, 3898 (1965).

[53] A. Perumal, V. Srinivas, V. V. Rao, and R. A. Dunlap, Phys. Rev. Lett. **91**, 137202 (2003).

[54] L. Zhang, D. Menzel, C. M. Jin, H. F. Du, M. Ge, C. J. Zhang, L. Pi, M. L. Tian, and Y. H. Zhang, Phys. Rev. B **91**, 024403 (2015).

[55] S. N. Kaul, J. Magn. Magn. Mater. **53**, 5 (1985).

[56] J. C. LeGuillou and J. Zinn-Justin, Phys. Rev. B **21**, 3976 (1980).

[57] A. Taroni, S. T. Bramwell, and P. C. Holdsworth, J. Phys.: Condens. Matter **20**, 275233 (2008).

[58] S. F. Fischer, S. N. Kaul, and H. Kronmuller, Phys. Rev. B **65**, 064443 (2002).

[59] M. E. Fisher, S. Ma, and B. G. Nickel, Phys. Rev. Lett. **29**, 917 (1972).

[60] J. G. Cheng, J. S. Zhou, J. B. Goodenough, and C. Q. Jin, Phys. Rev. B **85**, 184430 (2012).

[61] E. P. Wohlfarth, J. Appl. Phys. **39**, 1061 (1968).

[62] Y. Takahashi, J. Phys. Soc. Jpn. **55**, 3553 (1986).

[63] M. Imai, C. Michioka, H. Ueda, and K. Yoshimura, Phys. Rev. B **91**, 184414 (2015).

[64] See Supplemental Material at http://link.aps.org/supplemental/10.1103/PhysRevB.109.094408 for a detailed analysis on the critical behavior of sample S2.

[65] V. K. Pecharsky and K. A. Gschneidner Jr., J. Magn. Magn. Mater. **200**, 44 (1999).

[66] D. Griffiths, *Introduction to Electrodynamics*, 3rd ed. (Prentice Hall, Englewood Cliffs, NJ, 1999), pp. 559–562.

[67] Y. Liu and C. Petrovic, Phys. Rev. B **98**, 064423 (2018)

[68] B. S. Wang, J. C. Lin, P. Tong, L. Zhang, W. J. Lu, X. B. Zhu, Z. R. Yang, W. H. Song, J. M. Dai, and Y. P. Sun, J. Appl. Phys. **108**, 093925 (2010).

[69] K. A. Gschneidner Jr., V. K. Pecharsky, A. O. Pecharsky, and C. B. Zimm, Mater. Sci. Forum **315-317**, 69 (1999).

[70] H. Oesterreicher and F. T. Parker, J. Appl. Phys. **55**, 4334 (1984).

[71] V. Franco, J. S. Blazquez, and A. Conde, Appl. Phys. Lett. **89**, 222512 (2006).

[72] Y. Sun, Z. Song, Q. Tang, and X. Luo, J. Phys. Chem. C **124**, 11110 (2020).

[73] W. Liu, Y. Wang, J. Fan, L. Pi, M. Ge, L. Zhang, and Y. Zhang, Phys. Rev. B **100**, 104403 (2019).

[74] Y. Liu and C. Petrovic, Phys. Rev. B **97**, 174418 (2018).

[75] J. Yan, X. Luo, F. C. Chen, J. J. Gao, Z. Z. Jiang, G. C. Zhao, Y. Sun, H. Y. Lv, S. J. Tian, Q. W. Yin, H. C. Lei, W. J. Lu, P. Tong, W. H. Song, X. B. Zhu, and Y. P. Sun, Phys. Rev. B **100**, 094402 (2019).

[76] V. Franco and A. Conde, Int. J. Refrig. **33**, 465 (2010).

[77] Y. Su, Y. Sui, J. G. Cheng, J. S. Zhou, X. Wang, Y. Wang, and J. B. Goodenough, Phys. Rev. B **87**, 195102 (2013).

[78] W. Liu, J. Zhao, F. Meng, A. Rahman, Y. Qin, J. Fan, L. Pi, Z. Tian, H. Du, L. Zhang, and Y. Zhang, Phys. Rev. B **103**, 214401 (2021).

[79] W. Liu, D. Liang, F. Meng, J. Zhao, W. Zhu, J. Fan, L. Pi, C. Zhang, L. Zhang, and Y. Zhang, Phys. Rev. B **102**, 174417 (2020).

[80] M. Neupane, M. M. Hosen, I. Belopolski, N. Wakeham, K. Dimitri, N. Dhakal, J.-X. Zhu, M. Z. Hasan, E. D. Bauer, and F. Ronning, J. Phys.: Condens. Matter **28**, 23LT02 (2016).

[81] Y. Wang, J. H. Yu, Y. Q. Wang, C. Y. Xi, L. S. Ling, S. L. Zhang, J. R. Wang, Y. M. Xiong, T. Han, H. Han, J. Yang, J. Gong, L. Luo, W. Tong, L. Zhang, Z. Qu, Y. Y. Han, W. K. Zhu, L. Pi, X. G. Wan, C. Zhang, and Y. Zhang, Phys. Rev. B **97**, 115133 (2018).

[82] G. Chang, B. Singh, S.-Y. Xu, G. Bian, S.-M. Huang, C.-H. Hsu, I. Belopolski, N. Alidoust, D. S. Sanchez, H. Zheng, H. Lu, X. Zhang, Y. Bian, T.-R. Chang, H.-T. Jeng, A. Bansil, H. Hsu, S. Jia, T. Neupert, H. Lin, and M. Z. Hasan, Phys. Rev. B **97**, 041104(R) (2018).